JOURNAL OF AIRCRAFT
Vol. 45, No. 3, May–June 2008

Computational Modeling of HART II Blade-Vortex Interaction Loading and Wake System

Joon W. Lim* and Roger C. Strawn*
Ames Research Center, Moffett Field, California 94035

DOI: 10.2514/1.31081

Correlations using a loosely coupled trim methodology of the computational fluid dynamics (OVERFLOW-2) and computational structural dynamics (CAMRAD-II) codes are presented to calculate the helicopter rotor blade-vortex interaction airloads and wake system for the higher-harmonic aeroacoustic rotor test (HART II) rotor at an advance ratio of 0.15. Five different grid models are studied to quantify the effects of grid refinement on rotor-wake resolution. The fine grid model has a total of 113 million grid points and it improves airload predictions compared with the standard grid model for three HART II test cases: baseline, minimum noise, and minimum vibration. The rotor-wake positions are well predicted by this fine grid model. The computed vorticity field for a young vortex using the fine grid model is compared with the measured particle image velocimetry data and the results are good. The fine grid model underpredicts the experimental value for the maximum vorticity by 61%. The predicted vortex core radius is 15% in chord for the fine grid while the measured data show about 5% chord length. The predicted swirl velocity is, however, higher than the measured data for this vortex. The results in this paper provide the first quantitative comparisons between the measured and computational fluid dynamics/computational structural dynamics computed flowfield for a helicopter rotor-wake system.

Nomenclature

C_n	=	section normal force
C_T	=	thrust coefficient
$\mathbf{L}$	=	airloads (lift, drag, and moment)
M_{tip}	=	hover tip Mach number
$\mathbf{Q}$	=	second invariant velocity gradient tensor
x_h	=	longitudinal position in the hub coordinate system, positive downstream, m
z_h	=	vertical position in the hub coordinate system, positive above the rotor, m
α_s	=	shaft angle, positive aft, deg
γ	=	vorticity, rad/s
θ_{3P}	=	3-per-rev pitch control magnitude, deg
ρ	=	vortex core radius, m
σ	=	solidity
ψ	=	rotor azimuth, deg
ψ_{3P}	=	3-per-rev pitch control phase, deg
ω	=	angular velocity, rad/s
$\propto$	=	advance ratio

I. Introduction

THE aerodynamic design problems associated with rotorcraft involve interactions between the rotating blades and their aerodynamic wake systems. Prediction of the rotor wake is one of the most challenging problems in rotorcraft computational fluid dynamics (CFD).

Successful modeling of the rotor wake depends on three key criteria. First, the rotor blade motion must be accurately modeled to get the starting points where the tip vortices are created. Second, the rotor blade loading must be accurately predicted to obtain the correct initial tip vortex strengths. Finally, the vortex wake system must be accurately convected through the computational domain without excessive numerical dissipation of the rotor tip vortices.

Recent advances [1–6] in coupling rotorcraft computational structural dynamics (CSD) to rotorcraft CFD have demonstrated significant progress in meeting these first two vortex modeling criteria. Coupled CFD/CSD airload solutions have been generated for cases with both steady-level and steady-descent flight conditions. Overall, results that include the CFD aerodynamics show significant improvements for the rotor blade motion and airloads prediction over the traditional lifting-line aerodynamics methods that are present in most helicopter comprehensive codes.

The results in this paper extend these recent advances in CFD/CSD coupling methodology to focus on detailed rotor-wake computations for cases with strong blade-vortex interaction (BVI). These blade-vortex interactions are a significant source of annoying and intrusive noise from helicopter rotors and this noise source becomes dominant during low-speed descent and maneuvering flights where the rotor wake is blown back into the rotor plane.

An extensive range of measured rotor-wake data is available for descending flights with strong BVI loadings. The higher-harmonic aeroacoustic rotor test (HART II) [7–9] was conducted in 2001 by researchers from the German Aerospace Center (DLR), the French Office National D'Etudes et de Recherches Aerospatiales (ONERA), the German–Dutch wind tunnel (DNW), NASA, and the U.S. Army Aeroflightdynamics Directorate (AFDD) using a 40% Mach-scaled model of a BO-105 main rotor in the open-jet anechoic test section of the German–Dutch wind tunnel (DNW). The goal for this test was to focus on the measurement of the rotor wake and vortex development. Measured data from this test included 3-components (3C) particle image velocimetry (PIV), stereo pattern recognition (SPR), blade tip deflection (BTD), rotor balance, noise measurements, and blade pressures. These data are key resources that can be used to investigate interactions of rotor dynamics, aerodynamics, and rotor-wake models as well as for improvement of the BVI airloads prediction.

The loose coupling methodology for CFD and CSD codes has previously been documented and validated in [1–5]. In addition, [6] has applied this CFD/CSD coupling technology to the HART II rotor with strong emphasis on comparisons of the predicted and experimental blade section airloads. However, extensive 3-C PIV measurements of rotor-wake geometry have not yet been computed with any of the predicted results from the CFD/CSD coupled

Presented as Paper 1281 at the 45th AIAA Aerospace Sciences Meeting and Exhibit, Reno, Nevada, 8–11 January 2007; received 16 March 2007; revision received 1 August 2007; accepted for publication 2 August 2007.

*Research Scientist, Aeroflightdynamics Directorate (AMRDEC), U.S. Army Research, Development and Engineering Command, M/S 215-1. Member AIAA.

calculations. Comparisons of rotor-wake geometry and tip vortex properties from the 3-C PIV measurements will provide improved physical understanding of the BVI rotor airloads. They will also help to assess the ability of current state-of-the-art CFD methods to accurately model the details of complex rotor wakes.

In addition to the CFD/CSD coupling methodology, the computations in this paper focus on using fine CFD grids to convect the rotor tip vortices with minimal numerical dissipation. Computed results for the vortex wake system are compared to experimental PIV wake measurements from the HART II rotor test [7–9]. The overall objective of this paper is to analyze and validate present CFD/CSD rotor-wake predictions using the HART II experimental database. Accuracy of the CFD/CSD rotor-wake predictions will be assessed through comparisons with data from three different HART II test conditions: baseline, minimum noise, and minimum vibration.

II. CFD/CSD Loose Coupling Analysis

The CFD/CSD loose coupling analysis is based on the strategy of replacing the two-dimensional steady-state airloads in typical CSD methods with three-dimensional unsteady airloads from CFD computations. Rotor trim as well as elastic blade motions is computed by the CSD code using the rotor airloads computed from the CFD analysis. The CSD code used in this study is CAMRAD-II [10], and the CFD code used for airload calculation is OVERFLOW-2 [11,12].

In the CSD model, the blade was discretized into 16 nonlinear beam elements (finite element), with smaller beam elements inboard to capture blade structural behavior accurately [13,14]. The beam element was represented by three translational (axial, lead–lag, flap) and three corresponding rotational degrees of freedom (DOF) and resulted in 15 DOFs for each beam element.

For the CFD aerodynamic model, the Reynolds-averaged Navier–Stokes computational fluid dynamics code, OVERFLOW-2, is employed. The OVERFLOW-2 solutions are computed on structured, overset grids having body-conforming near-body (NB) grids and Cartesian off-body (OB) grids [12]. Near-body grids consist of discretized 3-dimensional meshes surrounding blade surface geometries and these grids are capable of capturing the wall-bounded viscous effects. Off-body grids consist of 3-dimensional background grids extended to the far field and are primarily for capturing the wake effects. These off-body grids are clustered in multiple levels with the finest grid spacing in the level 1 mesh that surrounds the rotor blades. The grid spacing increases by a factor of 2 for each successive off-body grid level up to the outer boundary.

In the loose coupling methodology [4,6], information between the CSD and CFD codes is exchanged once per rotor revolution on a periodic basis as shown in Fig. 1. For periodic rotor solutions, these information exchanges are more efficient than tight coupling between CFD and CSD at every time step.

The coupling iterations begin with the CSD baseline calculation of the rotor motions trimmed using airloads ($\mathbf{L}^{\mathrm{LL}}$) from a two-dimensional lifting-line method. Trimmed rotor motions are then passed to the CFD code, which computes a new set of airloads using these blade motions. The newly calculated CFD airloads ($\mathbf{L}^{\mathrm{CFD}}$) are transferred back to the CSD code to obtain a new trimmed rotor solution. These CFD airloads include the lift, drag, and pitching moment at the aerodynamic computation points along the blade span.

For the subsequent CFD/CSD iterations, new CSD airloads are computed using the relation,

$$\mathbf{L}_i^{\mathrm{CSD}} = \mathbf{L}_i^{\mathrm{LL}} + \left(\mathbf{L}_{i-1}^{\mathrm{CFD}} - \mathbf{L}_{i-1}^{\mathrm{LL}}\right) \tag{1}$$

where i is the ith coupling trim iteration, and the trim is recomputed with updated CSD airloads. Figure 1 shows the details of this CFD/CSD coupling trim process. As the CFD/CSD coupling trim iterations reach convergence, only the CFD airloads are used for the trimmed CSD airloads ($\mathbf{L}_i^{\mathrm{CSD}} = \mathbf{L}_i^{\mathrm{CFD}}$). Therefore, the trimmed CSD airloads are obtained entirely from the unsteady and three-dimensional CFD solution.

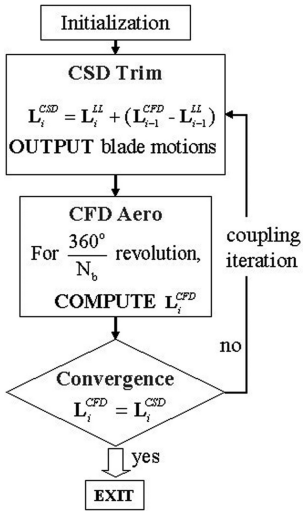

Fig. 1 CFD/CSD loose coupling algorithm.

The loose coupling methodology has already been demonstrated in [6,15] for the HART II rotor system with generally good comparisons between experimental and computed rotor airloads. Detailed comparisons between the experimental and computed rotor-wake system were not performed, however, and this subject will be addressed in the remainder of this paper. The HART II measured dataset contains extensive laser PIV measurements of rotor-wake geometry and strength and these data will be explored using the CFD or CFD/CSD predicted results.

III. HART II CFD Model Details

The HART II rotor is a 40% Mach-scaled model of the BO-105 hingeless rotor, operating at a nominal speed of 1040 rpm. The rotor has four blades, each having a radius of 2 m with a constant chord of 0.121 m and a linear twist of −8 deg. The rotor blade has a modified NACA 23012 airfoil having a trailing-edge tab with a length of 5.4 mm and thickness of 0.8 mm. The near-body grid uses an O-mesh topology. Three different near-body meshes (coarse, standard, and fine) have been used for the HART II rotor blade, and the blade standard and fine meshes are shown in Fig. 2. The fine mesh for the near-body grid uses high resolution in the trailing-edge region of the O mesh in an attempt to improve the accuracy of the computed drag.

Grid generation for the HART II rotor uses the overset near-body/off-body discretization concept. Each blade grid system consists of three near-body grids: blade grid, root cap, and tip cap. Note that the rotor hub is not modeled in the CFD grid. The complete rotor model includes the near-body grids for all four blades. The near-body grids extend slightly more than one chord away from the blade surfaces in the normal direction.

For the Cartesian off-body grid system, the standard grid has a level-1 off-body uniform grid spacing of 0.10 chords in the region around the rotor blades. The fine OB grid contains approximately 8 times the number of the standard off-body grid points with a level-1 grid spacing of 0.05 chords close to the rotor blades. The coarse off-body grid has a level-1 grid spacing of 0.20 chords.

Table 1 describes the grid sizes used for the HART II CFD grid models. The coarse grid system contains the coarse near-body and coarse off-body grids (cnb/cob), and has a total of 2.9 M (million) grid points after combining the near-body and off-body grids for all four blades. The standard grid system (snb/sob) has a total of 19.4 M grid points, while the fine grid system (fnb/fob) has 112.9 M grid points. Different combinations of near-body and off-body grids are used for the calculations to explore the effectiveness of the different meshes, and higher grid resolutions are meant to enhance the resolution of the rotor wake for a more accurate representation of BVI airloads.

Because of numerical stability limitations for the CFD model, an azimuthal step size of 0.05 deg (7200 steps per revolution) is used

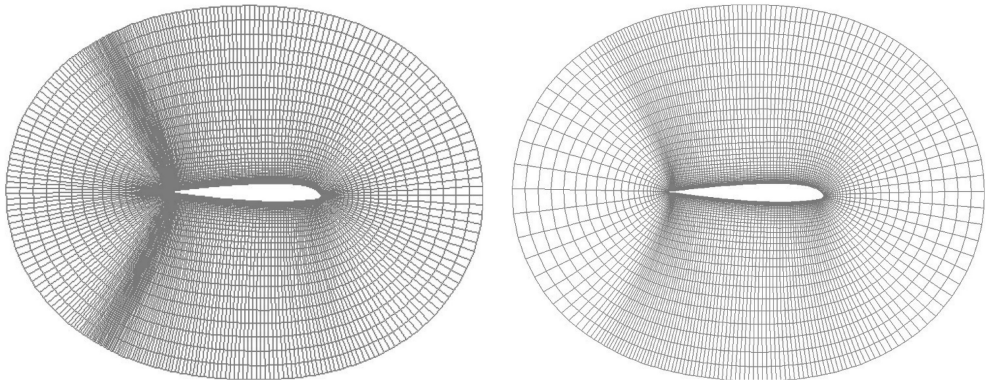

a) Fine mesh (295 × 80 × 65) b) Standard mesh (201 × 78 × 65)

Fig. 2 HART II blade near-body volume grids.

with an implicit first-order temporal scheme in all CFD calculations. The OVERFLOW-2 input uses fourth-order spatial central differencing with standard second- and fourth-order artificial dissipation in the near-body grids. The turbulence effect is modeled using the Spalart–Allmaras one-equation turbulence model. For the off-body grids, the fourth-order spatial central differencing scheme is used with inviscid modeling for reduced artificial dissipation.

IV. HART II PIV Setup and Vortex Identification

Figure 3 shows all the equipment set up for the HART II 3-C PIV measurement, including three double-pulsed Nd:YAG lasers and five digital cameras was mounted onto a remote controlled traverse system. This traverse system was located outside of the shear layer of the wind tunnel in the open-jet configuration and moved in the direction of flow, so that the distance between the camera and the light sheet plane remains constant. A total of four cameras have been used to collect 3-C PIV data. One pair of cameras has 100 mm lenses (DNW measurement window) for a larger observation area and the other pair has 300 mm lenses (DLR measurement window) to investigate the tip vortex with high spatial resolution.

The remaining lasers and cameras have been used to determine the precise location of tip vortices before taking data with the 3-C PIV cameras. The entire traverse system was moved to the opposite side of the wind tunnel to measure the wake on the retreating side. Further details of the test setup and measuring techniques are given in [16,17].

The locations and orientations of the measuring cut planes over the rotor disk are shown in Fig. 4. In each PIV measuring plane (black line segment), 100 instantaneous PIV images are obtained. These line segments have specific orientations with respect to the wind tunnel x axis (positive downstream) in the x–y plane. For the advancing side, this orientation angle is 149.35 deg and for the retreating side, this angle is 30.06 deg. As shown in Fig. 4, the reference blade position for the PIV measurements in the second and fourth quadrants is a 70 deg azimuth angle. For the first and third quadrants, the reference blade is located at 20 deg.

The strength and geometry of the computational rotor tip vortices can be evaluated from the primitive velocity values with a similar procedure to what was used for the experimental data. However, this task is much easier for the computational solution because there is no experimental uncertainty in the computations and the vortex structures are truly periodic from one revolution to the next.

For the computational solution, vorticity values are computed normal to prescribed two-dimensional cutting planes in the rotor-wake system. The centers of the discrete vortices are indicated by local maxima in the vorticity magnitude. This procedure follows the recommendations of Strawn and Kenwright [18], who have successfully used this criterion of local maxima in vorticity magnitude for the identification of vortex centers in rotary-wing CFD solutions. Other vortex identification criteria, such as centers of swirling flow [19], have also been used to identify vortex centers in CFD solutions. However, these techniques do not work well for typical rotary-wing CFD datasets. Strawn and Kenwright [18] demonstrate that the center of swirl method for vortex identification does not clearly distinguish between multiple vortices with overlapping rotational cores, and the local vorticity maxima method for vortex identification gives correct results for vortex identification.

Table 1 Comparison of the grid sizes for the HART II CFD grid models (unit = million grid points)

	NB	OB	Total
Coarse grids (cnb/cob)	0.9	2.0	2.9
Standard grids (snb/sob)	6.8	12.6	19.4
Fine grids (fnb/fob)	12.1	100.8	112.9
Fine NB/std OB (fnb/sob)	12.1	12.6	24.7
Standard NB/fine OB (snb/fob)	6.8	100.8	107.6

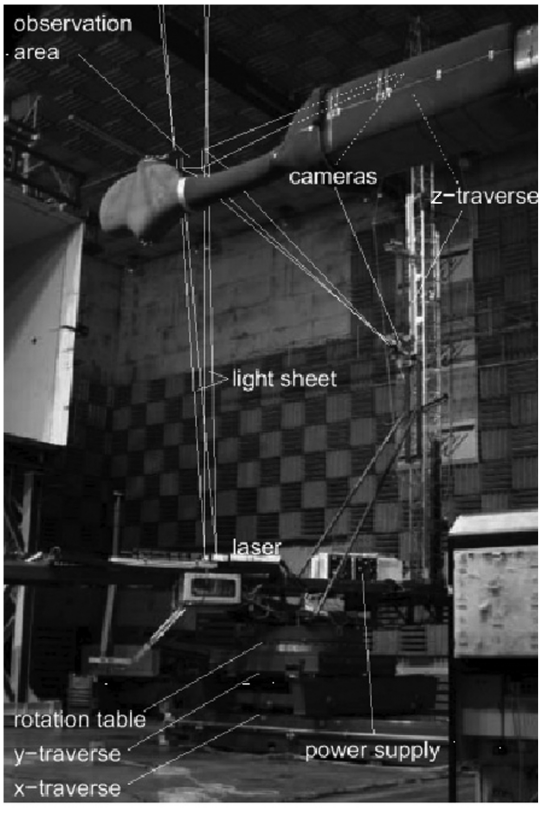

Fig. 3 HART rotor and 3-C PIV test setup.

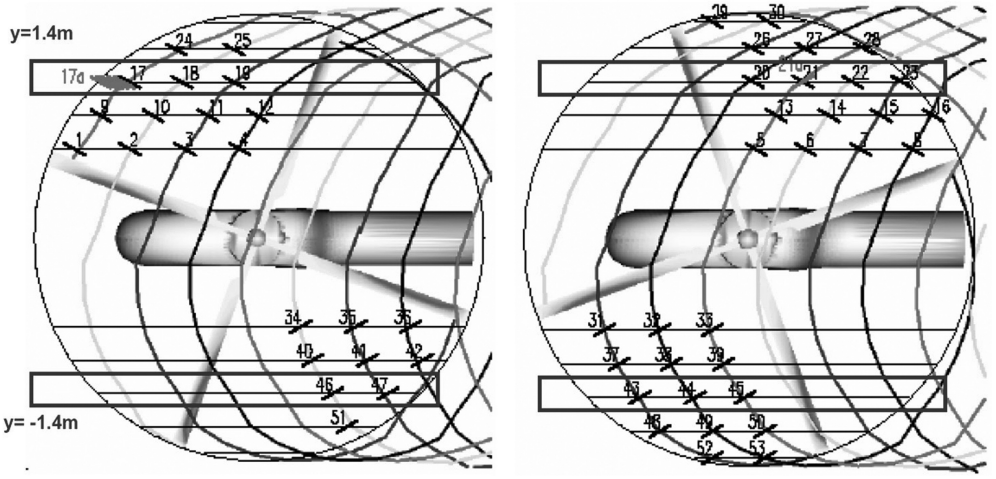

a) Ψ=70° b) Ψ=20°

Fig. 4 HART II PIV measurement plane positions for the baseline case.

V. Results and Discussion

Three representative HART II rotor cases (baseline, minimum noise, and minimum vibration) have been used for validation of the BVI-induced rotor flowfield. For these cases, the rotor has a shaft tilt of 5.3 deg with a thrust level (C_T/σ) of 0.050–0.056 at an advance ratio of 0.15. The minimum noise and minimum vibration cases were set up by adding 3-per-rev pitch controls over the baseline. Using these cases, the aerodynamics and vortex properties will be investigated through airload comparisons and flowfield visualization.

A. Rotor Airload Prediction

Figure 5 shows the $M^2\ C_n$ prediction at 87% blade span for the HART II baseline case (BL) at an advance ratio of 0.15 and demonstrates the sensitivity to different grid resolutions. Five different combinations of the grid resolutions are compared with the measured data using the coarse, standard, and fine grids for the near body (nb) and the off body (ob). The measured data given by the symbols are conditionally averaged [20].

All five grid models accurately predict the 3-per-rev harmonics of $M^2\ C_n$, although the mean values are off from the measured data. The measured data indicate that strong BVI-induced higher-harmonic airloads appear in the first and fourth quadrants of the rotor. All of the computations accurately predict this BVI loading, except for the case having the coarse near-body and coarse off-body (cnb/cob) grids. In fact, the airload predictions using the coarse grid completely miss the higher-harmonic BVI loading. The models having the fine off-body grid (snb/fob, fnb/fob) show improved predictions of the BVI airloads compared with those having the standard off-body grid (snb/sob, fnb/sob).

The $M^2\ C_n$ predictions at 87% blade span for the minimum noise (MN) and minimum vibration (MV) cases are compared in Fig. 6 with the measured data. These predictions include only the cases having the standard near-body/off-body grid (snb/sob) and the fine near-body/off-body grid (fnb/fob) models. Similar to the BL case, the measured $M^2\ C_n$ data for the MN and MV cases shows strong higher-harmonic BVI loading in the first and fourth quadrants. Though both predictions are able to capture the higher-harmonic loading in the measured data, the fine grid (fnb/fob) model gives better prediction of this loading.

The thrust is calculated by summing the blade airloads over the rotor revolution, and the blade airloads are formed from integrating the section airloads along the blade span. Table 2 shows a comparison of the measured and predicted rotor forces and moments for the baseline case, trimmed from the CFD/CSD loose coupling analysis. Individual integrated forces are shown for both the CFD code (OVERFLOW-2) and the CSD code (CAMRAD-II). Although Table 2 shows some discrepancies between the CFD and CSD moments, these moment values are actually very small in absolute

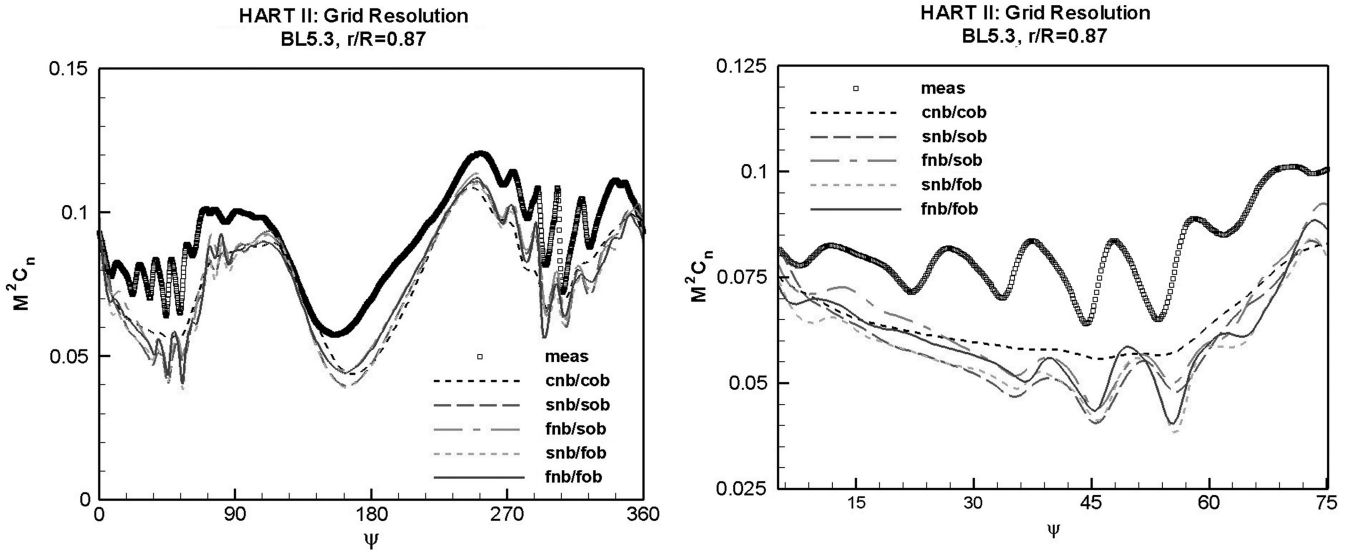

Fig. 5 M^2C_n at 87% blade span for the HART II baseline at an advance ratio of 0.15, computed using various grid resolution.

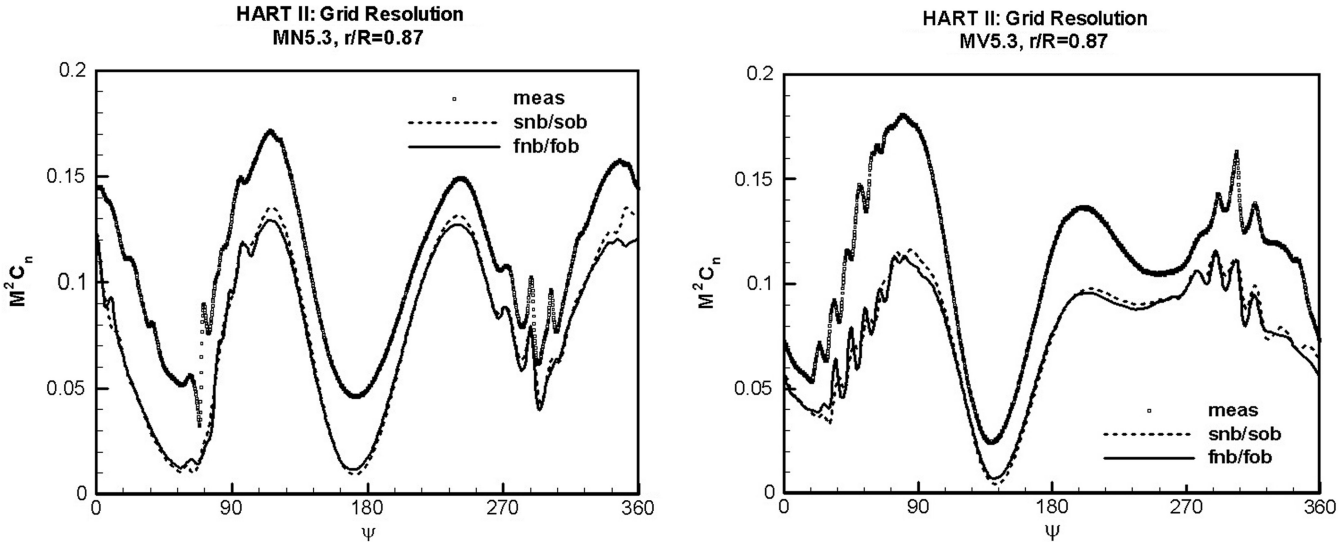

a) MN case **b) MV case**

Fig. 6 M^2C_n at 87% blade span for the HART II minimum noise (MN) and minimum vibration (MV) cases at an advance ratio of 0.15, computed using various grid resolution.

magnitude and the differences between the CFD and CSD moment values are within the CAMRAD-II trim tolerance range.

B. Rotor-Wake Position Predictions

Figure 7 shows the top and side views of the tip vortex wake trailers computed from the CFD/CSD coupled trim for the HART II BL case. The vortex wake representation is made using isosurfaces of the second invariant velocity gradient tensor, **Q** [21], computed using the standard near-body/fine off-body grids. In the side view, the isosurfaces of the vortex wake trailers are shown along with the vorticity contour in a longitudinal cutting plane located at $y/R = 0.7$ ($y = 1.4$ m) in the wind-tunnel coordinate system when the reference blade is at an azimuth of 0 deg. A majority of the tip vortex trailers in the first and fourth quadrants stay above the rotor plane, and the root vortices stay close along the blade span around the 0 deg azimuth angle as they are convected downstream. This rotor-wake visualization shows significant details of the rotor blade-vortex interactions, despite the fact that the computational mesh size is not nearly fine enough to completely convect the rotor wake without excessive numerical dissipation.

Measured and predicted tip vortex positions in longitudinal cutting planes at $y = 1.4$ m (advancing side) and $y = -1.4$ m (retreating side) are compared in Fig. 8 for the BL case. The measured data represent the vortex centers that have been identified from the simply averaged DNW PIV image [8]. The vortices on the advancing side are for the PIV measuring plane positions 17–23, and those on the retreating side are for the PIV positions 43–47, as seen in Fig. 4. The vortices in the second quadrant (positions 17–19) and the third quadrant (positions 43–45) are relatively young vortices, while those in the first quadrant (positions 20–23) and the fourth quadrant (positions 44–45) come from much older vortices.

The predicted tip vortex positions in Fig. 8 include the CFD/CSD results from the models using the fine grids (fnb/fob) and the standard grids (snb/sob). Both predictions on the advancing side are good in the upstream of the hub. However, the predictions show larger deviations from the measured data downstream of the hub. The vortex location predicted by the standard grid (snb/sob) model differs from its experimental counterpart by about one chord length (0.121 m) while the fine grid (fnb/fob) model shows an improved prediction compared to the standard (snb/sob) case.

The predictions on the retreating side show that the error in the predicted tip vortex locations is within a half chord length compared to the experimental values, which is better than those on the advancing side. Note that the snb/fob model shows a better prediction than the fnb/fob model at these vortex locations.

Figure 9 compares the predicted and measured tip vortex positions for the MN case in the longitudinal cutting locations at the $y = \pm 1.4$ m. Note that the measured data are not available for the position 23 on the advancing side and the positions 44 and 46 on the retreating side. The predictions correlate well with the measured data on both the advancing and retreating sides.

The rotor-wake field for the MV case is much more complex due to presence of the dual-tip vortices on the advancing side. These dual-tip vortices arise because the rotor blades have positive loading inboard and negative loading near the blade tips. Figure 10 shows the fine grid (fnb/fob) rotor-wake field computed by OVERFLOW-2 in the longitudinal plane at $y = \pm 1.4$ m when the reference blade is at 110 deg azimuthal angle. On the advancing side, the primary tip vortices show a negative vortex strength while the secondary tip vortices have an equally strong or even stronger positive vortex strength. These tip vortices are accompanied by strong shear layers with corresponding positive and negative vorticity. Note that these

Table 2 Comparison of the trimmed rotor forces and moments for the HART II BL case

	Measured	C-II	O2
Thrust, N	3308	3313	3304
Roll mom, N · m	−15	−18	16
Pitch mom, N · m	−25	−27	1
Yaw mom, N · m	−169	−254	−250

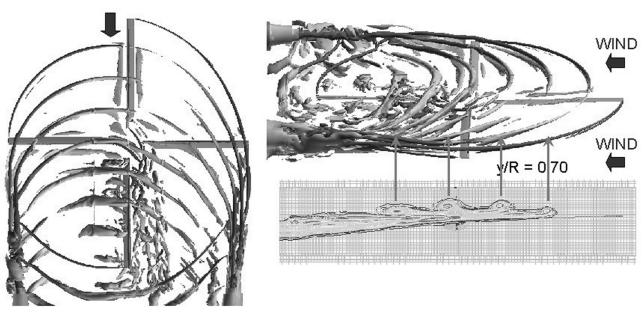

Fig. 7 Visualization of HART II rotor vortex trailers identified by isosurfaces of Q.

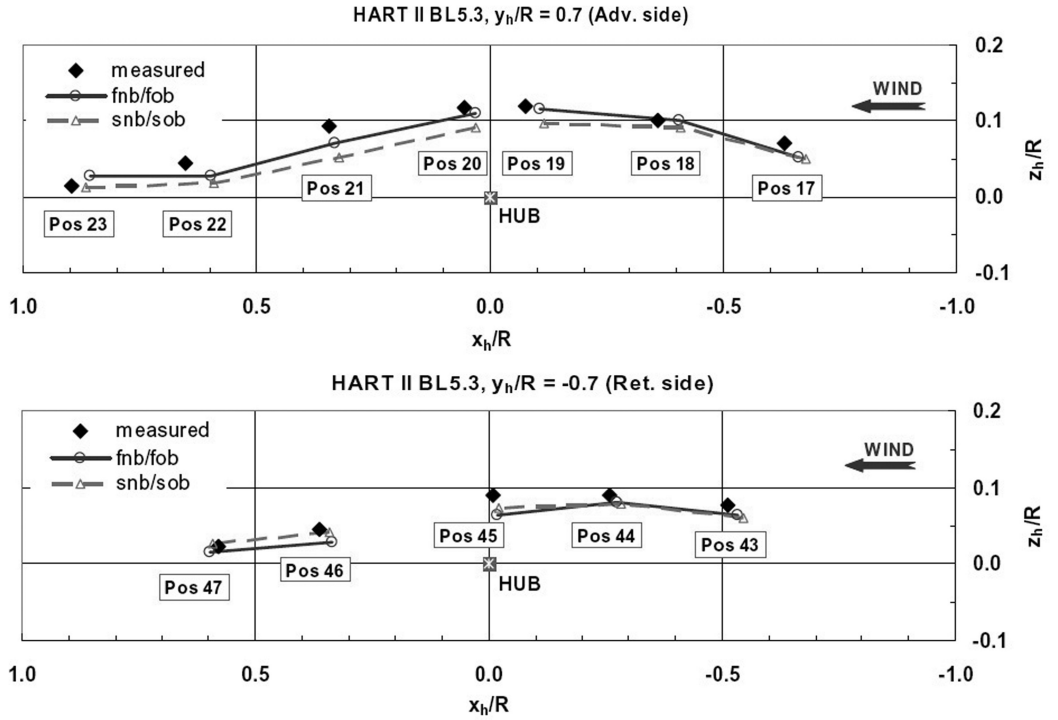

Fig. 8 Comparison of the vortex locations in the longitudinal cutting plane ($y_h/R = \pm 0.7$) on the advancing and retreating sides for the baseline case (chord/$R = 0.0605$).

dual vortices as a pair are not necessarily initiated from the same blade. On the retreating side, the tip vortices with a positive strength evolve clearly side by side.

Figure 11 shows the predicted and measured tip vortex positions for the MV case. The measured data come from PIV positions 18–22, and the measurements for the positions 17 and 23 were skipped during the test. For the advancing side, the predicted results for vortex positions correlate very well with the measured data, except at the most downstream position 22 where the predicted vortex position is less than one chord length from the rotor blades. The prediction on the retreating side compares very well with the measured data.

C. Vortex Flowfield Analysis

Figure 12 shows one instantaneous image taken by two different cameras for the data point, Dpt 995 at position 21. The upper image (0.45 m × 0.38 m) shows the larger, raw data image view taken from the DNW camera. This DNW image shows the apparent center of the

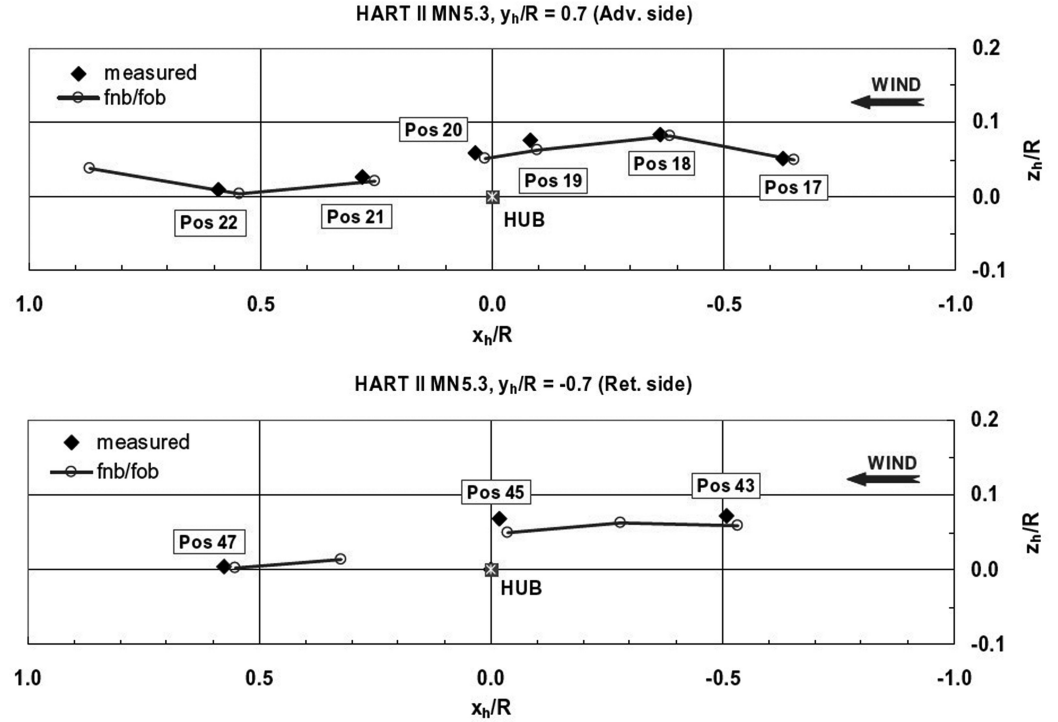

Fig. 9 Comparison of the vortex locations in the longitudinal cutting plane ($y_h/R = \pm 0.7$) on the advancing and retreating sides for the minimum noise case (chord/$R = 0.0605$).

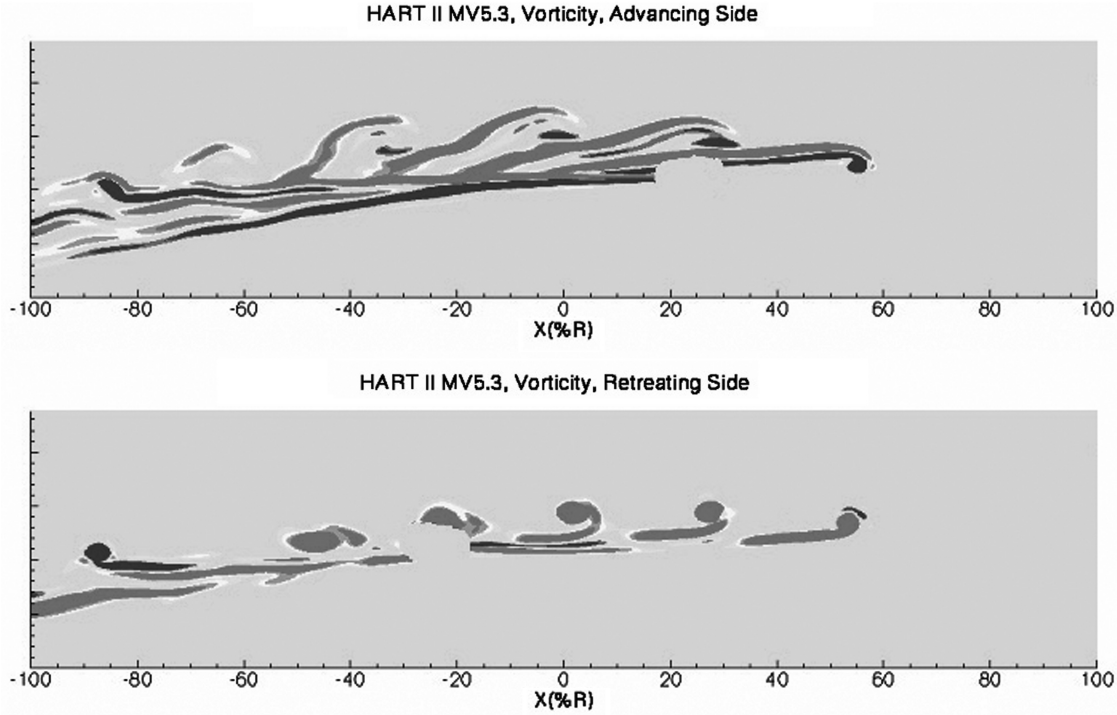

Fig. 10 Rotor-wake field computed by OVERFLOW-2 having the fnb/fob grids in the longitudinal plane at $y_h/R = \pm 0.7$ when the reference blade is at 110 deg.

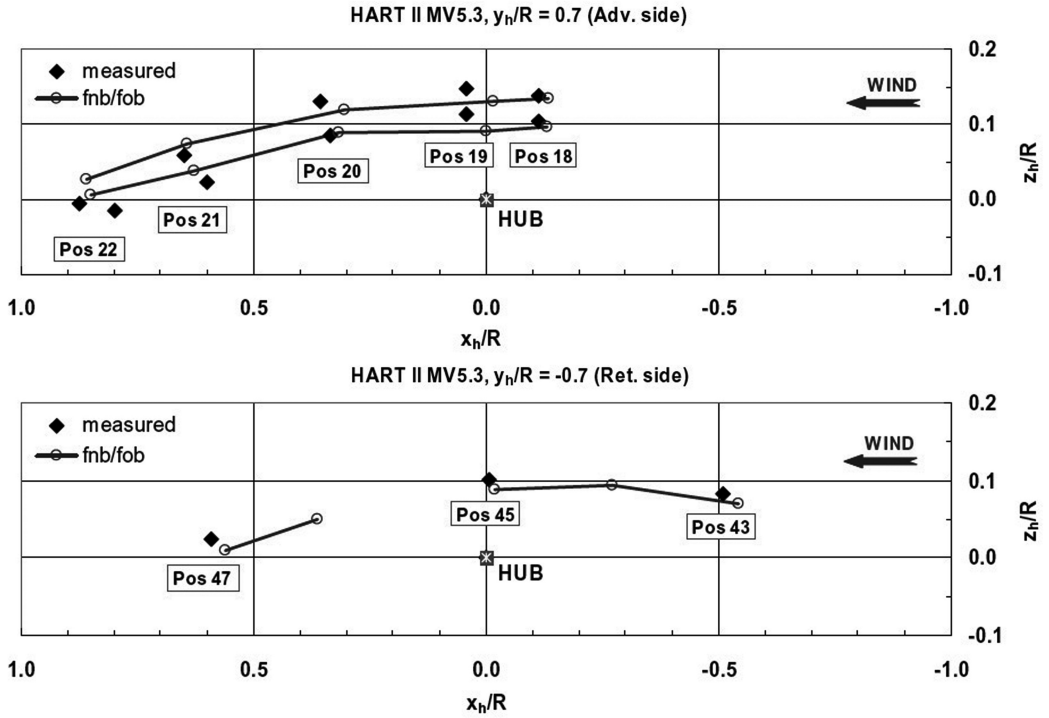

Fig. 11 Comparison of the vortex locations in the longitudinal cutting plane ($y_h/R = \pm 0.7$) on the advancing and retreating sides for the minimum vibration case (chord$/R = 0.0605$).

vortex swirl motion in the flowfield, and these DNW data could be used for vortex position estimates.

But, it was found [22] that the PIV image resolution was not sufficiently high enough to ensure a high quality of the 3-component velocities in the flowfield of the DNW PIV measurement window. The close-up image (0.15 m × 0.13 m) from the DLR camera is a subset of the larger DNW image with higher resolution, and these DLR data have been used to enhance the quality of the flowfield velocities for subsequent analysis of the vortex properties.

The vortex center is generally characterized by the maximum vorticity from the vorticity field contour. The vorticity field, γ, is derived using the equation, $\gamma = 2\,\omega_z = \mathbf{k} \cdot (\text{curl}\,\mathbf{V})$ where ω_z is the angular velocity and $\mathbf{V}$ is a vector of the 3-components of the local PIV data velocities. The coordinate system employed here is the local PIV coordinate system collocated at the origin of the PIV measuring plane, having the x axis positive to the right direction from the observer, the y axis positive up, and the z axis positive toward the observer.

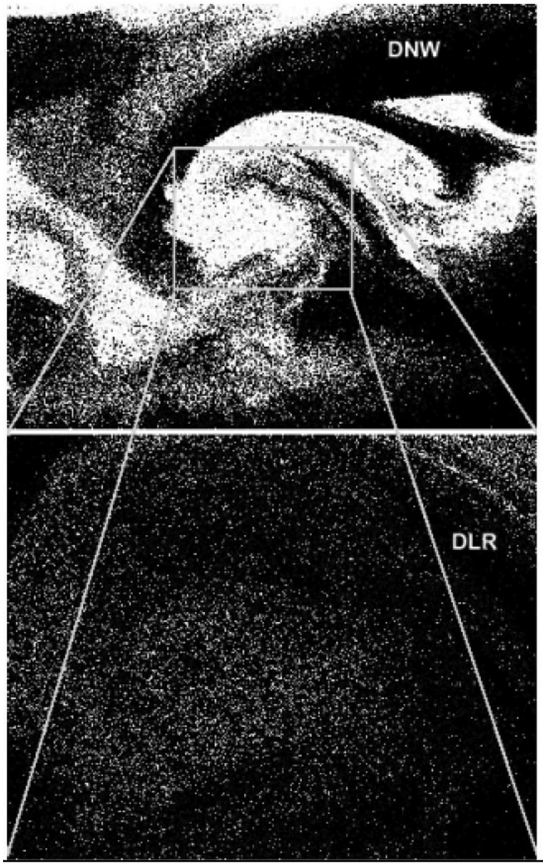

Fig. 12 Raw data image from two different cameras for the BL case, position 21.

Figure 13 compares the vorticity fields for the PIV measurement position 17 in the HART II baseline case. Figure 14 shows close-ups of the same vorticity field. The measured data in Figs. 13a and 14a show the PIV images obtained using the simple average technique [21,23] from 100, individual DLR PIV images. The vortex center is identified by the maximum vorticity, and the vortex in the figure is accompanied with a strong shear layer having about one-third of the maximum vorticity strength. The vortex at this PIV position is a young tip vortex that was initiated from the preceding blade located at an azimuth of 135.6 deg and convected downstream with a wake age of 25.3 deg. This young vortex appears as a strong, concentrated vortex before full growth, and is easily recognized without difficulty.

The vorticity field in Figs. 13 and 14 is predicted using two different grid models (fnb/sob and fnb/fob). Earlier in Fig. 8, we found that the error between predicted and experimental tip vortex locations for the PIV position 17 is less than one chord length. Along with these generally good predictions of the vortex position, the two predicted CFD vorticity distributions in Figs. 13 and 14 are also similar to the measured data. However, the contour levels for the standard OB grid model (fnb/sob) appear smaller than the measured data, and the maximum vorticity strength is much lower. This lower maximum vorticity value is caused by the insufficient grid resolution around the vortex core that produces excessive numerical dissipation. This situation is substantially improved with the fine OB grid model (fnb/fob) as shown in Figs. 13c and 14c.

Note that the predicted results in Figs. 13 and 14 show an elliptic vorticity distribution around the vortex center. This elliptic vorticity distribution is resulted from the fact that this PIV image plane is not exactly normal to the vortex trajectory axis. A small rotation of the PIV image would generally yield a circular vorticity distribution.

The vorticity field contour in Fig. 13c predicted by the fine grid model (fnb/fob) shows the dual tip vortices which are not seen in the measured data. This is due to the fact that the M_2 C_n computed by OVERFLOW-2 contains a small negative blade loading in the

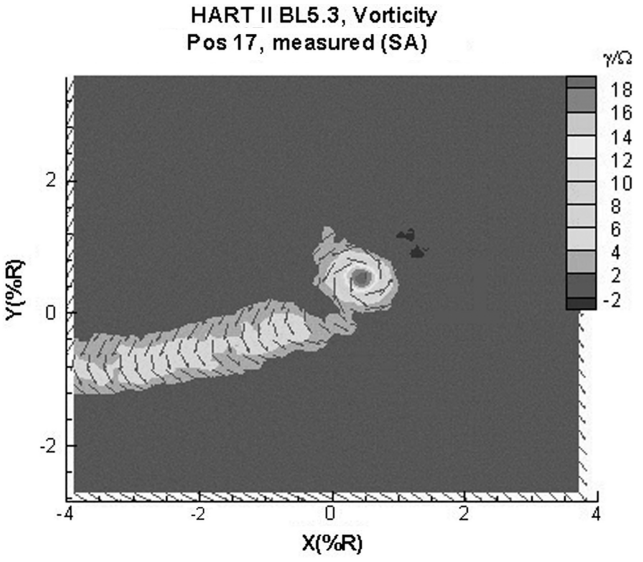

a) Measured data

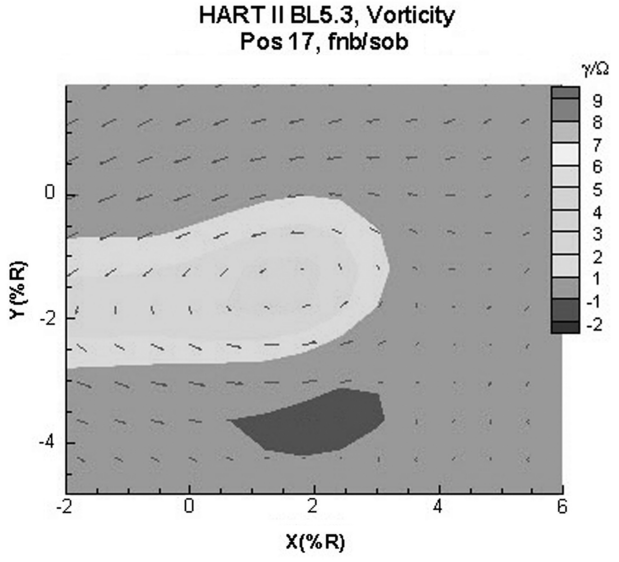

b) Fine NB/standard OB grids

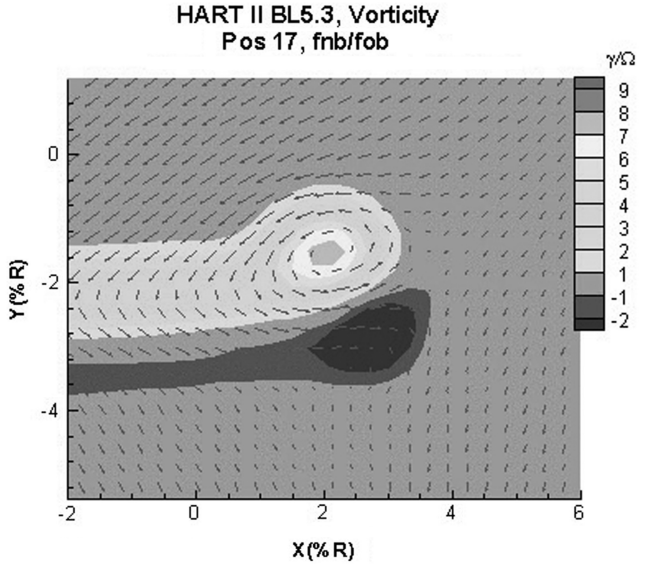

c) Fine NB/fine OB grids

Fig. 13 Comparison of vorticity and in-plane velocities for HART II BL, position 17.

outside of the 99.2% blade span for the azimuths of 146–174 deg where this PIV measurement position 17 is located closely.

As mentioned earlier, Fig. 14 shows a close-up of the sub-region near the vortex core. To extract the swirl velocities, the 3-components velocities were filtered by subtracting the vortex center velocities from the flowfield velocities in the PIV plane. The resulting swirl velocities in Fig. 14 show these filtered in-plane velocities, and all of the images show a clear swirl motion around the vortex center. The spacing of the grid lines in Figs. 14b and 14c indicates the actual mesh sizes used for the CFD computation. The mesh size in the standard OB grid (fnb/sob) is clearly too coarse to accurately capture the vortex details and, while the fnb/fob grid model shows a substantial improvement, is still not fine enough.

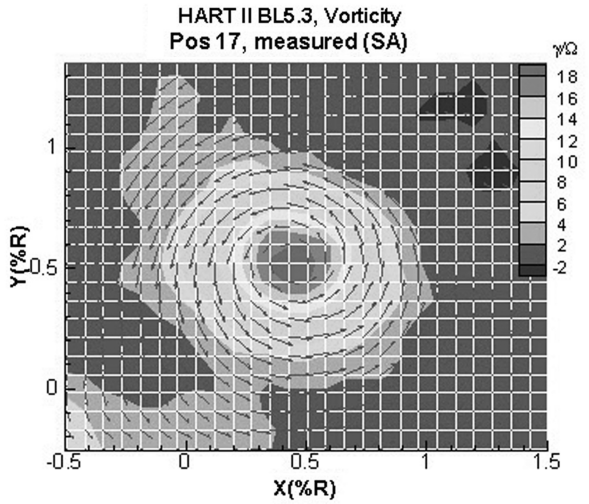

a) Measured data

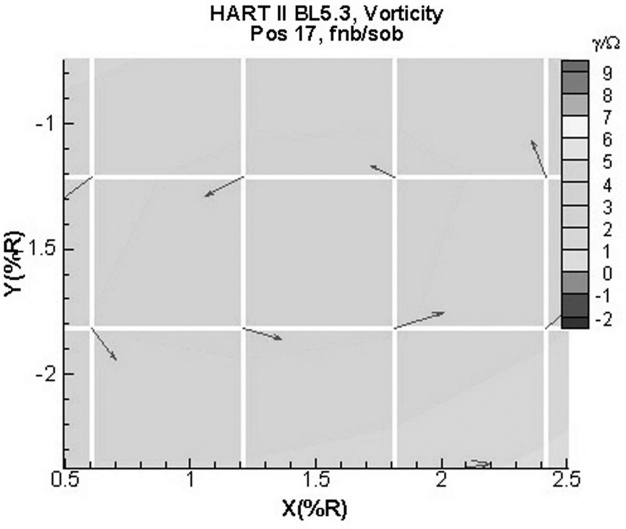

b) Fine NB/standard OB grids

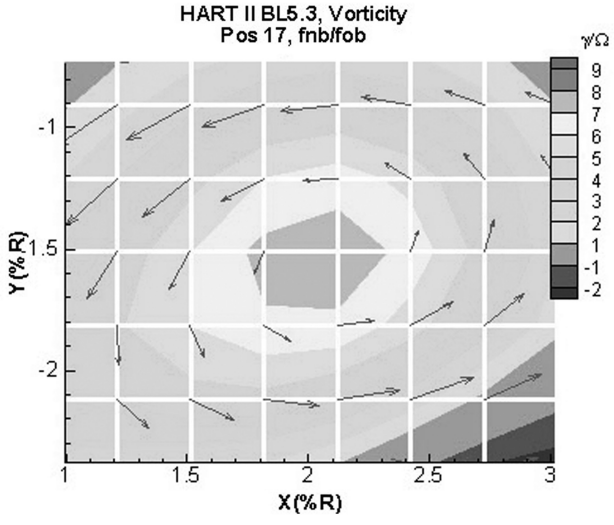

c) Fine NB/standard OB grids

Fig. 14 Comparison of vorticity and in-plane velocities for HART II BL, position 17 (close-up view).

The measured crossflow velocity distributions are one of the factors used to judge the need for rotation of the PIV image plane to have it perpendicular to the tip vortex trajectory. Predicted crossflow fields for the PIV position 17 are compared with the measured data in Fig. 15. This figure shows similar crossflow contour patterns for the measured data and predicted results. Note that the measured data indicate a small imbalance in the crossflow field which may indicate the need for an addition small rotation of the PIV image.

The vorticity strength for the HART II BL case at position 17 is compared in Fig. 16a along the vortex core radial distance. Because the PIV image is unrotated, a small correction in the magnitude of the maximum swirl velocity may be required to account for the vorticity field normal to the vortex trajectory. As observed earlier in Fig. 14, the predicted maximum vorticity magnitudes are poor compared to the measured data but better than one's expectation. Because of excessive numerical dissipation from inadequate resolution in the CFD mesh, Fig. 16a shows that the standard OB grid (fnb/sob) model predicts 17% of the measured maximum vorticity and the fine OB grid (fnb/fob) model predicts 39% of the measured maximum vorticity.

Figure 16b also compares the measured and predicted vortex swirl velocities. The measured data indicate that this young vortex has the vortex core radius of about 5% chord length (0.28%R), while the predictions compute it substantially higher at 15% (0.9%R) and 23% (1.4%R) chord lengths, respectively, for the fine OB (fnb/fob) and the standard OB (fnb/sob) grid models. The maximum swirl velocity magnitude is about 2.5% of the rotor tip speed for the measured data, and reasonably predicted for both grid models. Note that the nominal magnitude of the swirl velocity in hover is about 15–25% of the rotor tip speed [24].

The individual symbols in Fig. 16 indicate the spacings for the measured data and the CFD meshes, and these spacings are visually depicted by the grid lines (white color) in Fig. 14. A comparison of these symbol spacings in Fig. 16 indicates that the fine off-body grid spacing must be decreased by about a factor of 4 in order to fully capture the details of the rotor-wake system with the same resolution as in the measured data.

The mesh spacing for the fine off-body grid model is 5% chord. It is expected that a reduction in mesh spacing to 1.25% of chord would greatly improve the CFD results for the vortex property analysis. The reduction in grid spacing would require approximately 7.2 billion total grid points. Such a grid system is too large to run on current high-performance parallel computers, but future improvements in computational algorithm efficiency and parallel computer speed should eventually turn this into a tractable problem.

VI. Conclusions

This paper presents CFD/CSD loose coupling results for the HART II rotor airloads and rotor-wake field with strong BVI conditions. Predicted results are compared to representative HART II test cases corresponding to the baseline, minimum noise, and minimum vibration conditions. The results in this paper provide the first comparisons between the measured and CFD/CSD computed wake solutions for the HART II rotor.

Overall, the inclusion of the unsteady and three-dimensional OVERFLOW-2 aerodynamics solutions into the CAMRAD-II code has significantly improved the airload predictions for the HART II rotor cases. In addition, the rotor-wake geometry and strength are well predicted by the CFD/CSD coupled calculation. With these

general points in mind, conclusions are made from the results presented:

1) Grid resolution has substantial effect on the fidelity of both the computed airloads and wake system. The coarse grid CFD calculations do not capture the high-frequency components of the BVI airloads. The use of a finer mesh for the near-body as well as off-body grids substantially improves the CFD results compare to the measured data. In fact, the fine grid model (fnb/fob) demonstrates significant improvement of $M^2 C_n$ especially for the minimum noise and minimum vibration cases, compared to the standard grid model. For the rotor-wake predictions, the finer CFD grid provides greatly enhanced resolution of the tip vortex strengths and velocity fields in the rotor wake, although the grid independence of the solution has not yet been achieved.

2) The rotor-wake positions are very well predicted by the fine grid model (fnb/fob) for the baseline, minimum noise, and minimum vibration cases.

3) The computed vorticity field of a young vortex in the HART II baseline case is compared with the measured PIV data and the results are poor but better than one's expectation. The computation underpredicts the measured data for maximum vorticity by 61% when using the fine grid model (fnb/fob).

4) The predicted vortex core radius is 15% in chord for the fine grid (fnb/fob) calculation while the measured data show about 5% chord length. The computational model reasonably predicts the maximum swirl velocity for this vortex compared to the measured data.

5) Using existing algorithms in OVERFLOW-2, a mesh size of 1.25% chord is estimated to capture the details of the rotor-wake system with the same resolution as in the measured data. This grid spacing is about 4 times finer in each direction than that used in the current fine off-body grids.

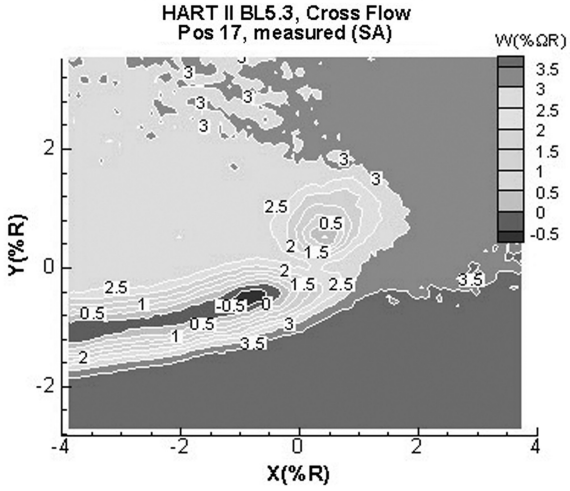

a) Measured data

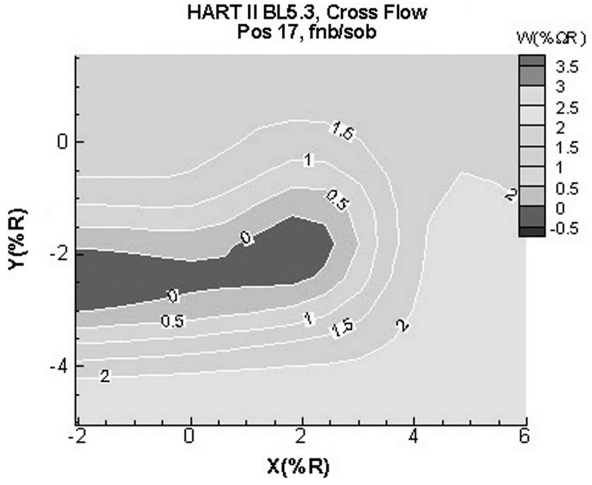

b) Fine NB/standard OB grids

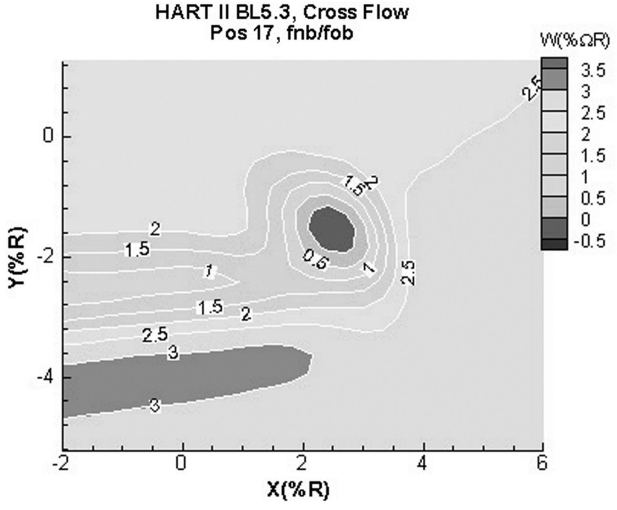

c) Fine NB/fine OB grids

Fig. 15 Comparison of crossflow for HART II BL, position 17.

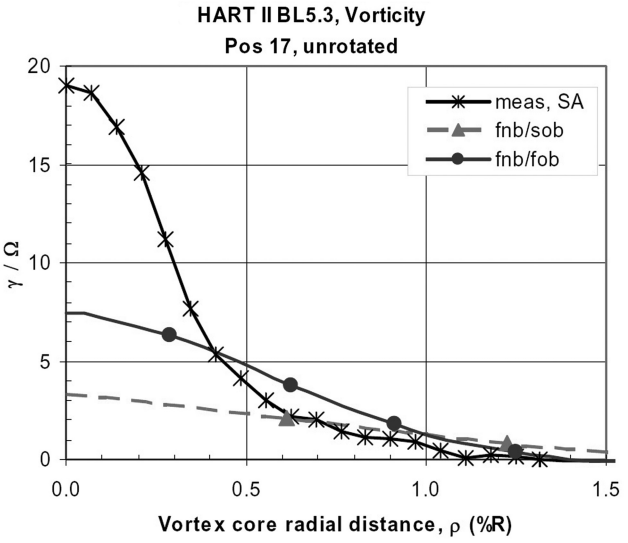

a) Vorticity

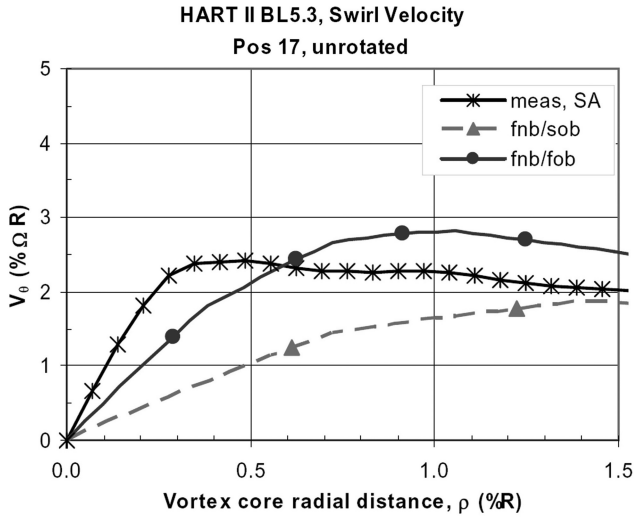

b) Swirl velocity

Fig. 16 Comparison of the vorticity strength and swirl velocity along the vortex core radius for HART II BL position 17.

Acknowledgments

The authors acknowledge the support of the HART II partners from the German Aerospace Center (DLR), the German–Dutch wind tunnel (DNW), NASA, and the Office National D'Etudes et de Recherches Aerospatiales (ONERA) with special thanks to Berend G. van der Wall of DLR and Casey L. Burley of NASA Langley Research Center. The authors also acknowledge invaluable guidance from Chee Tung (a retiree from Aeroflightdynamics Directorate, Ames Research Center) for physical insights of the vortex flowfields.

References

[1] Servera, G., Beaumier, P., and Costes, M., "A Weak Coupling Method Between the Dynamics Code HOST and the 3D Unsteady Euler Code WAVES," *Proceedings of the 26th European Rotorcraft Forum*, Sept. 2000.

[2] Pahlke, K., and van der Wall, B., "Calculation of Multibladed Rotors in High-Speed Forward Flight with Weak Fluid- Structure-Coupling," *Proceedings of the 27th European Rotorcraft Forum*, Sept. 2001.

[3] Sitaraman, J., Baeder, J., and Chopra, I., "Validation of UH-60A Rotor Blade Aerodynamic Characteristics Using CFD," *Proceedings of the American Helicopter Society 59th Annual Forum*, American Helicopter Society, Alexandria, VA, May 2003.

[4] Potsdam, M., Yeo, H., and Johnson, W., "Rotor Airloads Prediction Using Loose Aerodynamic/Structural Coupling," *Journal of Aircraft*, Vol. 43, No. 3, May–June 2006, pp. 732–742. doi:10.2514/1.14006

[5] Datta, A., Sitaraman, J., Chopra, I., and Baeder, J. D., "CFD/CSD Prediction of Rotor Vibratory Loads in High-Speed Flight," *Journal of Aircraft*, Vol. 43, No. 6, Nov.–Dec. 2006, pp. 1698–1709. doi:10.2514/1.18915

[6] Lim, J., Nygaard, T. A., Strawn, R., and Potsdam, M., "Blade-Vortex Interaction Airloads Prediction Using Coupled Computational Fluid and Structural Dynamics," *Journal of the American Helicopter Society*, Vol. 52, No. 4, Oct. 2007, pp. 318–328.

[7] Yu, Y. H., Tung, C., van der Wall, B. G., Pausder, H., Burley, C., Brooks, T., Beaumier, P., Delrieux, Y., Mercker, E., and Pengel, K., "The HART-II Test: Rotor Wakes and Aeroacoustics with Higher-Harmonic Pitch Control (HHC) Inputs—The Joint German/French/Dutch/US Project," *Proceedings of the American Helicopter Society 58th Annual Forum*, American Helicopter Society, Alexandria, VA, June 2002.

[8] van der Wall, B. G., Junker, B., Burley, C. L., Brooks, T., Yu, Y. H., Tung, C., Raffel, M., Richard, H., Wagner, W., Mercker, E., Pengel, K., Holthusen, H., Beaumier, P., and Prieur, J., "The HART-II Test in the LLF of the DNW-A Major StepTowards Rotor Wake Understanding," *Proceedings of the 28th European Rotorcraft Forum*, Sept. 2002.

[9] Burley, C. L., Brooks, T. F., van der Wall, B., Richard, H., Raffel, M., Beaumier, P., Lim, J., Yu, Y. H., Tung, C., and Pengel, K., "Rotor Wake Vortex Definition and Validation from 3-C PIV HART-II Study," *Proceedings of the 28th European Rotorcraft Forum*, Sept. 2002.

[10] Johnson, W., "Influence of Wake Models on Calculated Tiltrotor Aerodynamics," *Proceedings of the American Helicopter Society Aerodynamics, Acoustics, and Testing and Evaluation Technical Specialists Meeting*, American Helicopter Society, Alexandria, VA, Jan. 2002.

[11] Meakin, R. L., "Automatic Off-Body Grid Generation for Domains of Arbitrary Size,," AIAA Paper 2001-2536, June 2001.

[12] Buning, P. G., Gomez, R. J., and Scallion, W. I., "CFD Approaches for Simulation of Wing-Body Stage Separation," AIAA Paper 2004-4838, Aug. 2004.

[13] Lim, J. W., Tung, C., and Yu, Y. H., "Prediction of Blade-Vortex Interaction Airloads with Higher-Harmonic Pitch Controls Using the 2GCHAS Comprehensive Code," *Journal of Pressure Vessel Technology*, Vol. 123, No. 4, Nov. 2001, pp. 469–474. doi:10.1115/1.1401025

[14] Lim, J. W., and van der Wall, B. G., "Investigation of the Effect of a Multiple Trailer Wake Model for Descending Flights," *Proceedings of the American Helicopter Society 61st Annual Forum*, American Helicopter Society, Alexandria, VA, June 2005.

[15] Sim, B. W., and Lim, J. W., "Blade-Vortex Interaction (BVI) Noise and Airload Prediction Using Loose Aerodynamic/Structural Coupling," *Proceedings of the American Helicopter Society 62nd Annual Forum*, American Helicopter Society, Alexandria, VA, May 2006.

[16] Raffel, M., Richard, H., Ehrenfried, K., van der Wall, B. G., Burley, C., Beaumier, P., McAlister, K., and Pengel, K., "Recording and Evaluation Methods of PIV Investigations on a Helicopter Rotor Model," *Experiments in Fluids*, Vol. 36, No. 1, 2004, pp. 146–156. doi:10.1007/s00348-003-0689-7

[17] Richard, H., and Raffel, M., "Rotor Wake Measurements: Full-Scale and Model Tests," *Proceedings of the American Helicopter Society 58th Annual Forum*, American Helicopter Society, Alexandria, VA, May 2002.

[18] Strawn, R. C., Kenwright, D. N., and Ahmad, J., "Computational Visualization of Vortex Wake Systems," *AIAA Journal*, Vol. 37, No. 4, April 1999, pp. 511–512.

[19] Sujudi, D., and Haimes, R., "Identification of Swirling Flow in 3-D vector Fields," AIAA Paper 95-1715, June 1995.

[20] Schneider, O., and van der Wall, B. G., "Conditionally Averaging of Pressure Data from HART II," DLR, Rept. IB-111- 2006/08, German Aerospace Center (DLR), Braunschweig, Germany, Jan. 2006.

[21] van der Wall, B. G., and Richard, H., "Analysis Methodology for 3C-PIV Data of Rotary Wing Vortices," *Experiments in Fluids*, Vol. 40, No. 5, 2006, pp. 798–812. doi:10.1007/s00348-006-0117-x

[22] van der Wall, B. G., and Burley, C. L., "2nd HHC Aeroacoustics Rotor Test (HART II)—Part 2: Representative Results," German Aerospace Center (DLR), Institute Rept. IB 111-2005/03, Braunschweig, Germany, Feb. 2005.

[23] Bailly, J., Delrieux, Y., and Beaumier, P., "HART II: Experimental Analysis and Validation of ONERA Methodology for the Prediction of Blade-Vortex Interaction," *Proceedings of the 30th European Rotorcraft Forum*, Sept. 2004.

[24] Richard, H., Bosbach, J., Henning, A., Raffel, M., Willert, C., and van der Wall, B. G., "2C and 3C PIV Measurements on a Rotor in Hover Condition," *Proceedings of the 13th International Symposium on Applications of Laser Techniques to Fluid Mechanics*, Paper 1122, Center for Innovation, Technology and Policy Research, Lisbon, Portugal, 26–29 June 2006.